Carbon 154 (2019) 497–502

Contents lists available at ScienceDirect

Carbon

journal homepage: www.elsevier.com/locate/carbon

Effect of defect-induced cooling on graphene hot-electron bolometers

Abdel El Fatimy [a, **, 1], Peize Han [a], Nicholas Quirk [a], Luke St. Marie [a], Matthew T. Dejarld [b], Rachael L. Myers-Ward [b], Kevin Daniels [c], Shojan Pavunny [b], D. Kurt Gaskill [b], Yigit Aytac [c], Thomas E. Murphy [c], Paola Barbara [a, *]

[a] Department of Physics, Georgetown University, Washington, DC, 20057, USA
[b] U.S. Naval Research Laboratory, Washington, DC, 20375, USA
[c] Institute for Research in Electronics and Applied Physics, University of Maryland, College Park, MD, 20742, USA

ARTICLE INFO

Article history:
Received 6 May 2019
Received in revised form
5 August 2019
Accepted 7 August 2019
Available online 8 August 2019

ABSTRACT

At high phonon temperature, defect-mediated electron-phonon collisions (supercollisions) in graphene allow for larger energy transfer and faster cooling of hot electrons than the normal, momentum-conserving electron-phonon collisions. Disorder also affects the heat flow between electrons and phonons at very low phonon temperature, where the phonon wavelength exceeds the mean free path. In both cases, the cooling rate is predicted to exhibit a characteristic cubic power law dependence on the electron temperature, markedly different from the T^4 dependence predicted for pristine graphene. The impact of defect-induced cooling on the performance of optoelectronic devices is still unclear. Here we study the cooling mechanism of hot-electron bolometers based on epitaxial graphene quantum dots where the defect density can be controlled with the fabrication process. The devices with high defect density exhibit the cubic power law. Defect-induced cooling yields a slower increase of the thermal conductance with increasing temperature, thereby greatly enhancing the device responsivity compared to devices with lower defect density and operating with normal-collision cooling.

1. Introduction

Understanding the effect of disorder on the relaxation dynamics of charge carriers is crucial for the operation of most graphene devices. When electrons absorb energy, they quickly thermalize via electron-electron collisions within a few tens of femtoseconds [1–3] and via emission of optical phonons ($\hbar\omega_{op} > 200$ meV) within a few hundreds of femtoseconds [4,5], reaching an electron temperature T_e that can be substantially higher than the temperature of the graphene lattice. Dissipation of energy via acoustic phonons yields much longer cooling times, from tens to hundreds of picoseconds [6,7]. This is because momentum conservation and the limited Fermi surface of a two-dimensional material like graphene severely constraint the maximum amount of energy that can be dissipated in a collision process. The most energetic acoustic phonons are emitted by electrons that are backscattered. For an electron with energy E, this maximum phonon energy is given by $\Delta E_{ph} = 2Ev_s/v_F$, where v_F is the Fermi velocity and v_s is the sound velocity in graphene. Since $v_F \sim 50\ v_s$, this energy loss is a few percent of the electronic energy and therefore it takes many collisions for electrons to cool down. The maximum energy transfer to acoustic phonons for electrons at the Fermi energy defines the Bloch-Grüneisen temperature, $T_{BG} = 2E_F v_s/(v_F K_B)$, a characteristic temperature that plays a role similar to the Debye temperature in three-dimensional conductors. At temperatures below T_{BG}, the normal-collision cooling is characterized by the power law $P = A\Sigma (T_e^4 - T_0^4)$, where $\Sigma = \frac{\pi^2 D^2 |E_F| K_B^4}{15\rho_M h^5 v_F^3 v_s^3}$ is a coupling constant, D is the deformation potential of graphene, ρ_M its mass density, A is the graphene area, T_0 is the temperature of the graphene lattice and P is the power absorbed by the graphene under optical or electrical (Joule) pumping [8,9]. (Here we are assuming that the system is in a steady state, $C_e\left(\frac{dT_e}{dt}\right) = P - Q = 0$, where C_e is the electronic heat capacity and the absorbed power P balances the energy loss Q due to electron cooling.) At higher temperatures, $T_{BG} \ll T_0$, $T_e \ll E_F/K_B$, the power is predicted to depend linearly on temperature, $P \propto (T_e - T_0)$ [9].

* Corresponding author.
** Corresponding author.
E-mail addresses: a.elfatimy@gmail.com (A. El Fatimy), Paola.Barbara@georgetown.edu (P. Barbara).
[1] Present Addresses: Ecole Centrale Casablanca, Bouskoura, Ville Verte, 27182, Casablanca, Morocco.

https://doi.org/10.1016/j.carbon.2019.08.019
0008-6223/

In the presence of defects, the momentum conservation constraints described above are relaxed, because defect-assisted collisions enable emission of phonons with higher energy and momentum than normal collisions [7]. This supercollision-cooling regime is characterized by faster cooling times and by a cubic power law in steady state, $P = A\,\Sigma_2\,(T_e^3 - T_0^3)$, where $\Sigma_2 = \frac{\zeta(3)D^2|E_F|K_B^3}{\pi^2\rho_M\hbar^4v_F^3v_s^2l_{mfp}}$, l_{mfp} is the mean free path and the Riemann zeta function $\zeta(3) \approx 1.2$ [7]. Previous work on CVD grown graphene [10] and exfoliated graphene [11] measured this cubic power law at temperatures higher than T_{BG}, where, in the presence of defects, the supercollisions are predicted to dominate over normal collisions [7]. Other work used pump-probe experiments on exfoliated graphene with the defect density systematically increased by exposure to near-infrared femtosecond pulses and showed that samples with higher defect density had faster cooling times [12]. For lower temperatures, $T_x < T_0$, $T_e < T_{BG}$, the cooling occurs via normal collision, with the dependence $P \propto (T_e^4 - T_0^4)$ [10] down to a crossover temperature $T_x = \frac{30\,\hbar\,v_s\,\zeta(3)}{\pi^2K_Bl_{mfp}}$ [13,14]. When the electron and phonon temperatures are lowered below T_x, the cooling power is predicted to regain a cubic law dependence $P = A\,\Sigma_3\,(T_e^3 - T_0^3)$, with $\Sigma_3 = 2\Sigma_2$ [13,14].

The importance of charge carrier cooling in graphene and how it is affected by the presence of defects goes well beyond understanding the basic physics of two-dimensional conductors because it impacts any application of this material for bolometry and photodetection [15–19]. Although the defect-induced cooling and the normal collision cooling were observed with the corresponding cubic and T^4 power law dependences [10,11,14,16,20–22], they were not observed in the same temperature range, making it difficult to directly compare the electronic thermal conductance in the two regimes and assess the effect of defects on the performance of hot electron devices.

Here we study high-performance bolometers based on quantum dots of epitaxial graphene on silicon carbide. We show that the defect density in the graphene and the cooling mechanism can be controlled by the fabrication process. We find that devices based on defective graphene exhibit defect-assisted cooling and yield higher responsivity over a wider dynamic range than devices made with graphene having low defect density and operating under normal collision cooling.

2. Results and discussion

We recently showed that quantum dots patterned from epitaxial graphene on SiC exhibit a very strong dependence of the electrical resistance on temperature, higher than 100 MΩ K^{-1}, yielding extraordinary values of bolometric responsivity, larger than 10^9 V W^{-1} [23,24]. At a temperature of a few kelvins the resistance of the dot is as high as several hundreds of MΩ for the smallest dots and it dominates the graphene electrical resistance (estimates of other contributions to the graphene electrical resistance as well a heat flow diagram of the device are discussed in the supplementary information section of our previous work [23]). When the graphene is irradiated with an optical source or heated by Joule power, the electron temperature raises in the whole graphene area. The electrical resistance depends exponentially on the electron temperature because electrons are thermally activated over the quantum confinement gap, which is determined by the dot diameter [23,24]. (The orientation of the devices with respect to the steps between adjacent crystal planes on the SiC substrates also affects the temperature dependence of the resistance, because they affect the current flow through the device [23]). Fig. 1(a) shows the resistance vs. temperature curves for three samples.

Typical current-voltage (IV) characteristics of the quantum dot devices are shown in Fig. 1(b). The IV curves are non-linear because, as the bias voltage increases, the device temperature increases due to Joule heating and the resistance decreases, corresponding to the resistance vs. temperature (R(T)) curves in Fig. 1(a). The inset in Fig. 1(b) shows the differential resistance as a function of Joule power, computed from the IV curves of the devices. By combining the data of the differential resistance vs. Joule power with the R(T) data, we readily obtain the dependence of the electron temperature on Joule power that can be used to investigate the cooling mechanism of the quantum dot devices.

Most of the devices studied here and in our previous work [23,24] were fabricated using a thin (30 nm of Au or Pd) metallic layer as a mask to pattern the quantum dots [23,25]. The metallic layer protected the graphene from contamination with photoresist and was removed using aqua regia as the last fabrication step [25]. We also fabricated a test device using a different fabrication process, where the graphene was patterned by using crosslinked PMMA instead of the metallic layer. The data for five different samples are shown in Fig. 2 (a), with the red symbols showing the data for the test sample patterned with PMMA and the black ones showing the data for four samples patterned using the thin metallic layer. To test the cubic power law, we plot these same data as T_e vs. $P^{1/3}$ in Fig. 2 (b). We find that, for $T_e > 7.5$ K (dotted line in Fig. 2 (b)), all the samples fabricated using the metal layer as a mask to pattern the quantum dots show a very good agreement with the cubic

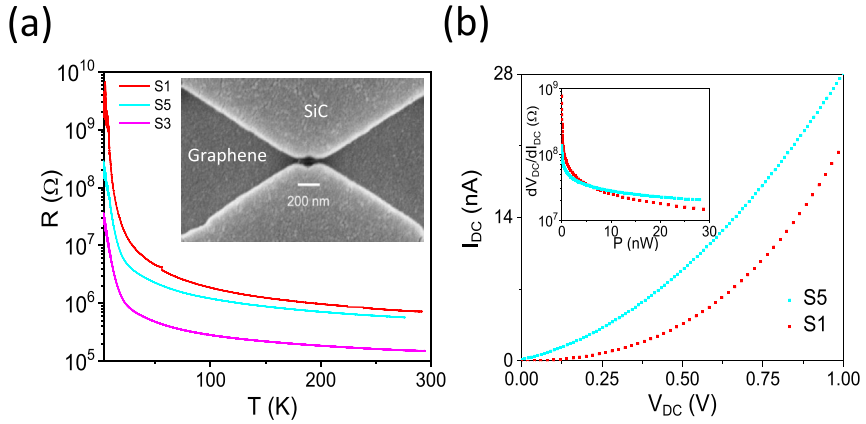

Fig. 1. (a) Resistance vs. temperature dependence for three quantum dot devices with diameters of 30 nm (S1), and 200 nm (S3 and S5). The data for device S1 are reproduced from Ref. [23]. (b) Current vs. voltage (IV) characteristics of two devices, at $T_0 = 3$K. The inset shows the differential resistance dV_{DC}/dI_{DC} as a function of Joule power ($P = I_{DC}\cdot V_{DC}$) obtained from the IV curves. (A colour version of this figure can be viewed online.)

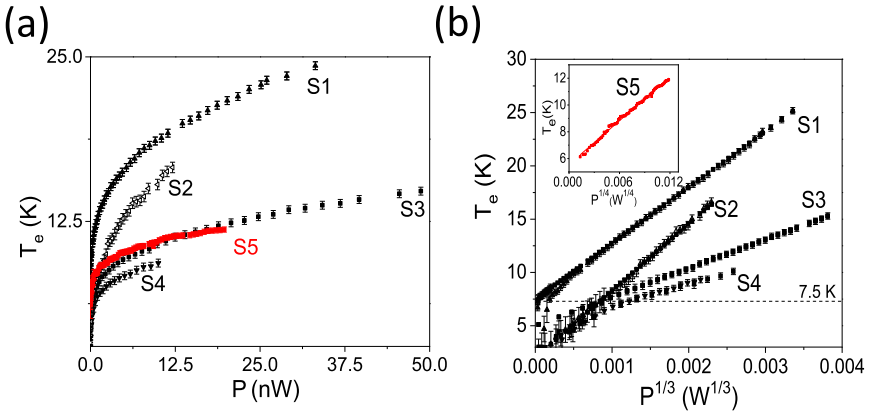

Fig. 2. (a) Electron temperature vs. Joule power for the sample patterned with overdosed PMMA (S5) and for the four samples patterned with a thin metallic layer (S1, S2, S3 and S4). (b) Data from (a) showing that T_e scales linearly with $P^{1/3}$ for samples S1, S2, S3 and S4 for $T_e > 7.5$ K. Inset: For sample S5, T_e scales linearly with $P^{1/4}$. (A colour version of this figure can be viewed online.)

power law, whereas the sample fabricated using the crosslinked PMMA, sample S5, shows a good agreement with the prediction for normal collision cooling, $P \propto T_e^4$ (see inset of Fig. 2(b)).

All the samples were fabricated using graphene epitaxially grown on SiC, but the different power laws clearly indicate that different fabrication procedures yield samples with different cooling mechanisms. The fabrication procedure can also affect the doping of the graphene. As-grown graphene on SiC typically exhibits n-type doping, with charge density of about $n \sim 10^{12}$ cm^{-2}, corresponding to $T_{BG} \sim 70$ K. This is consistent with the power law dependence expected for normal collisions in the low-temperature regime and measured for the sample fabricated using the overdosed PMMA. Conversely, the doping level of the graphene samples fabricated using the thin metal layer is expected to be quite different, due to the aqua regia treatment used to remove the metal layer. The aqua regia is a p-dopant for graphene [25], therefore the charge carrier density and value of T_{BG} can be quite different for the samples fabricated with the thin metal layer.

Although all the samples operated roughly in the same temperature range, T_0, $T_e < 30$ K, the cubic temperature dependence of the samples fabricated using the metal layer mask indicates that 1) the cooling mechanism is dominated by defects and 2) the samples could either be in the low-temperature regime, with T_0, $T_e < T_x$, or in the high temperature regime, with T_0, $T_e > T_{BG}$. Since T_{BG} depends on the graphene charge density via E_F, it is important to investigate how the different fabrication processes may affect the defect density and the doping of graphene.

Fig. 3 (a) shows the Raman spectra of samples S3 and S4 fabricated using the sputtered thin metallic layer, after subtracting the Raman spectrum of the SiC substrate. The Raman spectra were measured with a Horiba LabRAM HR Evolution, with a 532 nm laser (Ventus 532 from Laser Quantum). The inset shows the spectrum of another test sample, S5′, made of graphene epitaxially grown on SiC, with a small area of graphene protected by a layer of overdosed PMMA (purple), using the same procedure we used for sample S5. A thin metallic layer was subsequently deposited on the whole sample S5′ and then removed with aqua regia. The Raman spectrum after this procedure is also shown in the inset (blue). Sample S5′ was fabricated to unambiguously test the effect of the metal deposition on the quality of the exposed graphene and compare it to the graphene protected by the PMMA layer, using graphene epitaxially grown on the same SiC substrate. The samples S3 and S4 clearly show the presence of a large defect (D) peak at 1350 cm^{-1}, higher than the G peak ($I_D/I_G = 1.3$). By contrast, the graphene covered with PMMA on sample S5′ shows no measurable D peak. On the same sample S5', the part of graphene that was not

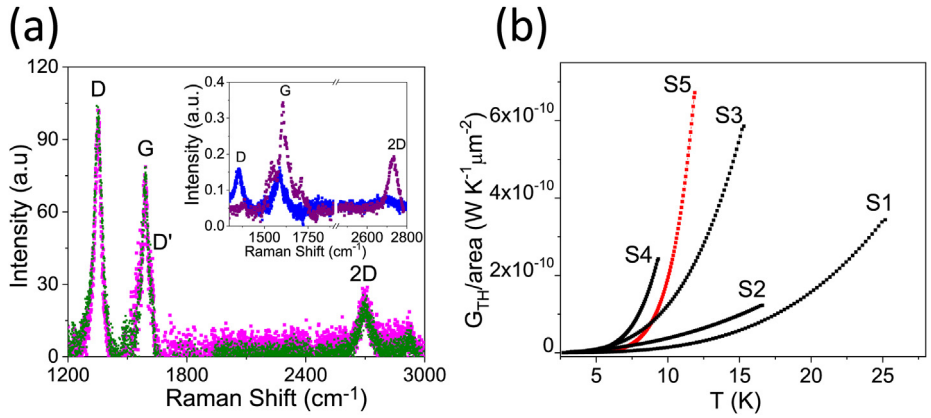

Fig. 3. (a) Raman spectra of samples S3 (pink) and S4 (green) after subtracting the SiC substrate. The inset shows the Raman spectra of sample S5′for the part protected with PMMA (purple) layer and the part processed with Au sputtering and aqua regia (blue). All spectra are taken at $E_L = 2.33$ eV ($\lambda_L = 532$ nm). (b) Thermal conductance per unit area for all the samples, obtained from the data in Fig. 2. The graphene area is about 20 μm^2 and it includes the graphene that is not covered by metal, i.e. the dot and the triangular source and drain graphene electrodes. (A colour version of this figure can be viewed online.)

Table 1
Characteristics of epitaxial graphene on SiC treated with different fabrication processes. The measurements were done at room temperature.

Fabrication process	Charge density (cm^{-2})	μ ($cm^2\ V^{-1}\ s^{-1}$)	l_{mfp} (nm)
SA (Pd sputtering and aqua regia)	$+5.6 \times 10^{12}$	51	1.3
SB (PMMA protection)	$- 3.4 \times 10^{12}$	260	5.3

protected with PMMA shows a substantially reduced intensity of the 2D peak and a large D peak ($I_D/I_G = 0.9$), similar to sample S3 and S4. For epitaxial graphene on SiC there is a contribution to the D peak from the buffer layer [18], but this is considerably smaller than the D peak found for the metal coated samples, thus indicating considerable reduction of sp2 symmetry caused by the presence of defects. For the PMMA-coated sample, the buffer layer contribution is similar in magnitude and shape to that reported by Fromm et al. [26] and observed for untreated pristine samples. Hence, there is little or no D peak for the PMMA coated sample. The data clearly indicate that the metal deposition introduced defects that were not present in the pristine or protected samples.

To further test the effects of the fabrication process on the defect density and doping, we divided a single sample of graphene epitaxially grown on SiC into three sections SA, SB, and SC, and processed each section differently. The graphene in section SA had a thin metallic layer sputtered on it and then removed with aqua regia, in the same way as during the fabrication of graphene quantum dots for samples S1, S2, S3, and S4. The graphene in section SB was patterned with overdosed PMMA, in the same manner as the fabrication of graphene quantum dots for sample S5. The graphene in section SC was removed by oxygen plasma etching, exposing the SiC substrate. We then measured the Raman spectrum of the graphene each section, as well as Hall effect to extract mobilities and carrier densities.

The Raman spectra of sections SA and SB are shown in Fig. 4(a), with the SiC background subtracted. Similar to the samples discussed in Fig. 3(a), the sample SA shows a substantial increase of the defect peak. The defects are induced in the graphene by the metal deposition and they depend on the deposition method, as described in the Supplementary Information. Values of the mobility and the doping level also differ substantially between the two regions, as shown in Table 1. The region treated with metal sputtering shows low mobility, about $51\ cm^2\ V^{-1}s^{-1}$, and very high hole doping, $5.6 \times 10^{12}\ cm^{-2}$, whereas the region protected with PMMA has mobility about five times higher, $260\ cm^2\ V^{-1}s^{-1}$, and electron doping with concentration typical for epitaxial graphene grown on SiC. It is clear that the sputtering and aqua regia process strongly dope the graphene with holes: it completely compensates the electron doping of the graphene epitaxially grown on SiC and further dopes it with holes, reaching charge density values comparable to the electron doping of the other region. The mean free paths for the two regions, $l_{mfp} = \mu\ (\pi n)^{1/2}\ (\hbar/e)$, where n is the charge carrier density and μ is the mobility, are also listed in Table 1.

We note that the short mean free paths indicate that our samples are in the high defect density regime, where the average distance between defects L_D cannot be accurately extracted from the Raman spectra using the empirical relation by Cançado et al.1 [27], which is valid for $L_D \geq 10$ nm. Using the values in Table 1, we can estimate the characteristic temperatures T_{BG} and T_x. Due to the similar values of charge carrier density, the values of T_{BG} are similar for the graphene treated with metal deposition and aqua regia and the graphene protected by PMMA (128 K and 100 K, respectively). The values of T_x are very different because of the different mean free paths, yielding $T_x = 42$ K for the graphene treated with Pd sputtering and aqua regia and a lower value, about 10 K, for the graphene protected with PMMA. This means that even though all the bolometers operate in the same temperature range, below 30K, those treated with metal sputtering and aqua regia operate in the low-temperature regime, with T_0, $T_e < T_x$, where the cubic power dependence holds, whereas the bolometer with the graphene protected by PMMA operates at temperatures very close to or higher than the crossover temperature T_x, where the temperature dependence for normal collisions dominates.

From the slopes of the T_e vs. $P^{1/3}$ plots, ranging from 0.18 to $6\ W\ K^{-3}m^{-2}$, we can extract the deformation potential D and find that it varies from 3 eV to 18 eV for the different samples treated with metal sputtering and aqua regia. These values are within the range found in other studies [10,28–30]. We also extracted the deformation potential from the slope of the T_e vs. $P^{1/4}$ of the PMMA-protected bolometer and found a larger value of D, about 40 eV, but still within the range of values found from previous work [11].

Having established that the quality of the graphene and the cooling mechanism can be controlled with the fabrication process, it is now important to understand which type of graphene and cooling mechanism will yield the best bolometric performance. Supercollision cooling yields faster devices, but its effect on one of the most important figures of merit, the bolometric responsivity, has not yet been explored. The responsivity is defined as the change of voltage ΔV_{DC} across the device caused by the incident light divided by the absorbed power, $r = \Delta V_{DC}/\Delta P = I_{DC}(\Delta R/\Delta P) = (I_{DC}/G_{TH})(\Delta R/\Delta T)$, where G_{TH} is the thermal conductance, ΔR is the change in resistance caused by a temperature increase ΔT and ΔV_{DC} is measured at a constant current I_{DC}. As discussed above and in our previous work [23,24], the temperature dependence of the quantum dot resistance is mainly determined by the quantum dot diameter, but the thermal conductance and its temperature dependence will strongly depend on the graphene quality and the graphene cooling mechanism. We can extract the thermal conductance directly from the data in Fig. 2 using $G_{TH} = dP/dT_e$. Fig. 3 (b) shows the thermal conductance as a function of temperature for all the samples discussed above. Although the values of thermal conductance of all the samples are comparable at low temperature, it is clear that the thermal conductance increases more slowly for the samples with supercollision cooling compared to the temperature dependence of the thermal conductance of the PMMA-protected sample undergoing normal collision cooling, as expected from the different exponents of the power law for the two different mechanisms. Since high responsivity requires lower thermal conductance, it is clear that the samples undergoing supercollision cooling will yield higher responsivity in a wider dynamic range.

So far we discussed the cooling properties of electrons in steady state, where the power absorbed from the incident radiation balances the energy lost via cooling. Now we focus on the regime where $C_e\left(\frac{dT_e}{dt}\right) = P - Q \neq 0$, to see how the defects induced by the different fabrication processes affect the cooling dynamics of electrons in graphene. We performed pump-probe measurements of the samples SA and SB at room temperature. The measurements were performed in the mid-IR spectral range, with wavelengths of the pump pulse set to 1.4 μm and the probe at 5.5 μm(see Fig. S1 in the Supplementary Information). The pump and probe were approximately 100 fs in duration, with radii (e^{-1} of the intensity) of

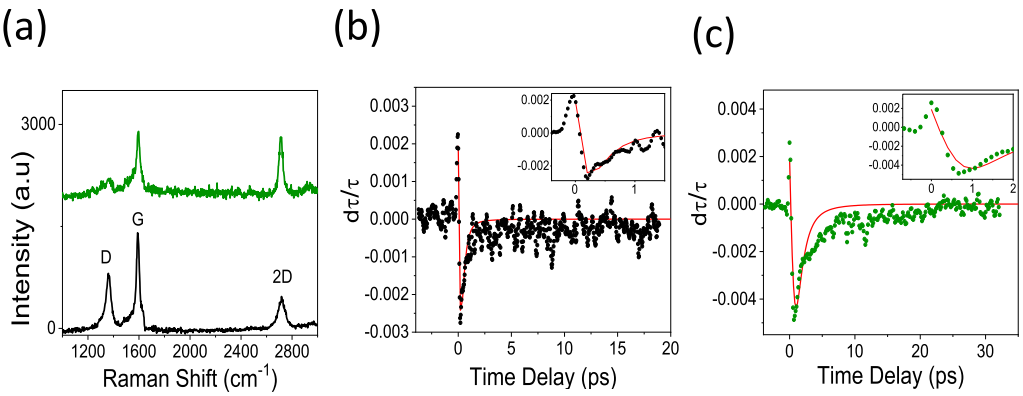

Figure 4. (a) Raman spectra of graphene on SiC substrates for two separate regions: region SA treated with Pd sputtering subsequently removed with aqua regia (black) and region SB with graphene protected with PMMA (green). The curves are shifted vertically for clarity. All spectra are taken at $E_L = 2.33$ eV ($\lambda_L = 532$ nm). (b) and (c) Time-resolved differential-transmission measurements for Pd sputtered (SA) and PMMA covered (SB) graphene on SiC, respectively, measured at room temperature. The red curves show fits to the data, using the model discussed in the text. The insets are enlargements of the graphs in the short time delay range. (A colour version of this figure can be viewed online.)

$\simeq$100 μm and $\simeq$35 μm, respectively, both much smaller than the size of the SA and SB regions, which ensures that the probe beam samples a spatially uniform region of photoexcitation. The pump and probe pulses were co-polarized, and co-focused at near-normal incidence angle on the graphene face of the surface. A small angle (approximately 4°) was introduced between the pump and probe, thereby permitting spatial separation of the transmitted far-field probe pulse from the incident pump pulse. A 5.5 μm bandpass filter was employed immediately after the difference frequency generation crystal to block the residual 1.4 μm and 2.0 μm radiation from the probe beam, and the transmitted probe pulses were measured using a cooled HgCdTe detector, which was preceded by a long-pass filter to extinguish any scattered pump radiation at 1.4 μm. Although the step-size of the mechanical delay stage used in the experiment was 33 fs, in practice the measurement resolution is limited to ~150 fs by the finite pump and probe pulse durations, which were each estimated to be 100 fs.

The time dependence of the differential transmission for sections SA and SB is shown in Fig. 4 (b) and (c), respectively. As explained in the supplemental material (Figs. S2–S4), the differential transmission shows positive values right after the pulse, when T_e is highest, then decreases sharply to negative values and reaches a minimum before increasing towards vanishing values. This non-monotonic time-dependence of the differential transmission can be used to extract information on the time dependence of the electron temperature. In the pump-probe measurements, the pump beam is optically chopped, while the probe beam is synchronously detected, thereby measuring the fractional change in transmission $\Delta\tau/\tau_0 = (\tau\text{-}\tau_0)/\tau_0$ as a function of the relative time difference between the pump and probe pulse, where τ_0 represents the optical transmission of the (room-temperature) graphene film in the absence of a pump pulse and τ is the time-dependent transmission under optical illumination. The mid-infrared optical transmission through the graphene sample depends implicitly on the electron temperature, through the relation $\tau = \frac{4Y_1Y_2}{|Y_1+Y_2+\sigma(\omega,\,T_e)|^2}$ [31], where Y_1 and Y_2 represent the admittances of the incident and substrate regions respectively, and $\sigma(\omega,T_e)$ is the complex conductivity of the graphene sheet, which is related to the temperature through the Kubo model [32]. The initial electron temperature, immediately following the absorption of the pump pulse, can be approximated as $T_{e,\,peak} = \left[T_0^2 + 2\frac{\eta\,P_{pump}}{\alpha\,\pi\,w^2}\right]^{1/2}$. Here $\alpha = \frac{C_e}{AT} = \frac{2\pi k_B^2 E_F}{3\,\hbar^2 v_F^2}$ is the heat capacity coefficient, η is the fractional absorption in the graphene film, P_{pump} is the pump power and w is the width of the optical beam at the focus. For the fluence and beam diameter used in the experiments, we estimate $T_{e,peak} = 10{,}000$ K. Assuming that supercollisions are the dominant cooling mechanism (we note that the pump-probe measurements are performed at room temperature, above T_{BG} for both SA and SB), the electron temperature relaxes to the lattice according to the dynamical equation: $\alpha T_e(t)\frac{dT_e(t)}{dt} + \Sigma_2[T_e(t)^3 - T_0^3] = 0$. Fig. 4(b) and (c) show the best fits to the data for samples SA and SB, using the parameters shown in Table 2.

When selecting the parameters to match the pump-probe data, we ignored the initial fast positive transient response prior to the dip in transmission, where other cooling mechanisms may contribute to the response [12,33] and the measurement resolution is insufficient to completely observe the dynamics. The mobility and charge carrier density values yielding the best fits are in very good agreement with the parameters independently measured by Hall measurements on the PMMA-covered sample (SB), whereas they are off by about a factor of two for the sample that was treated with Pd sputtering (SA). We note that the pump probe measurements were performed about one month before the transport measurements and the sample properties might have slightly deteriorated for the unprotected sample SA, due to sample handling and its exposure to ambient conditions. Nevertheless, the pump probe measurements confirm that the cooling coefficient $\sum_2$ is higher for the sample treated with Pd sputtering, leading to a faster response time and consistent with a shorter mean free path and higher defect concentration [7,12]. Moreover, the values of obtained Σ_2 from the pump-probe measurements are well within the range of the values obtained from the linear fits of T_e vs. $P^{1/3}$ from the transport measurements of the quantum dot bolometer samples in Fig. 2(b).

Table 2
Parameters used for the temperature model fits on time resolved measurements in Fig. 4(b) and (c).

	SB (PMMA Covered)	SA (Pd sputtering and aqua regia)
$n_0(cm^{-2})$	-3.4×10^{12}	11×10^{12}
μ (cm^2/Vs)	260	90
l (nm)	5.4	3.5
α (J/m^2K^2)	1.2×10^{-9}	2.2×10^{-9}
$\Sigma_2(W/m^2K^3)$	0.28	1.3

3. Conclusions

In summary, we studied the cooling mechanism of graphene epitaxially grown on SiC. We show that the fabrication process, including the deposition of thin metallic layers and exposure to aqua regia, substantially affects the defect density and the cooling mechanism. We find that the combination of faster response time and lower thermal conductance in a wide range of power and temperature make defective graphene the best material for bolometric applications.

Acknowledgements

This work was supported by the US Office of Naval Research (N00014-16-1-2674) and the NSF (ECCS-1610953). Research at NRL is supported by the Office of Naval Research. Matt and Shojan are grateful for support through the ASEE Postdoctoral Program.

Appendix A. Supplementary data

Supplementary data to this article can be found online at https://doi.org/10.1016/j.carbon.2019.08.019.

References

[1] M. Breusing, S. Kuehn, T. Winzer, E. Malic, F. Milde, N. Severin, J.P. Rabe, C. Ropers, A. Knorr, T. Elsaesser, Ultrafast nonequilibrium carrier dynamics in a single graphene layer, Phys. Rev. B (2011) 83.
[2] K.J. Tielrooij, J.C.W. Song, S.A. Jensen, A. Centeno, A. Pesquera, A.Z. Elorza, M. Bonn, L.S. Levitov, F.H.L. Koppens, Photoexcitation cascade and multiple hot-carrier generation in graphene, Nat. Phys. 9 (2013) 248–252.
[3] D. Brida, A. Tomadin, C. Manzoni, Y.J. Kim, A. Lombardo, S. Milana, R.R. Nair, K.S. Novoselov, A.C. Ferrari, G. Cerullo, M. Polini, Ultrafast collinear scattering and carrier multiplication in graphene, Nat. Commun. 4 (2013).
[4] D. Sun, Z.K. Wu, C. Divin, X.B. Li, C. Berger, W.A. de Heer, P.N. First, T.B. Norris, Ultrafast relaxation of excited Dirac fermions in epitaxial graphene using optical differential transmission spectroscopy, Phys. Rev. Lett. 101 (2008).
[5] H.N. Wang, J.H. Strait, P.A. George, S. Shivaraman, V.B. Shields, M. Chandrashekhar, J. Hwang, F. Rana, M.G. Spencer, C.S. Ruiz-Vargas, J. Park, Ultrafast relaxation dynamics of hot optical phonons in graphene, Appl. Phys. Lett. 96 (2010).
[6] E. Malic, T. Winzer, E. Bobkin, A. Knorr, Microscopic theory of absorption and ultrafast many-particle kinetics in graphene, Phys. Rev. B (2011) 84.
[7] J.C.W. Song, M.Y. Reizer, L.S. Levitov, Disorder-assisted electron-phonon scattering and cooling pathways in graphene, Phys. Rev. Lett. 109 (2012).
[8] K. Kaasbjerg, K.S. Bhargavi, S.S. Kubakaddi, Hot-electron cooling by acoustic and optical phonons in monolayers of MoS2 and other transition-metal dichalcogenides, Phys. Rev. B 90 (2014).
[9] J.K. Viljas, T.T. Heikkila, Electron-phonon heat transfer in monolayer and bilayer graphene, Phys. Rev. B (2010) 81.
[10] M.W. Graham, S.F. Shi, D.C. Ralph, J. Park, P.L. McEuen, Photocurrent measurements of supercollision cooling in graphene, Nat. Phys. 9 (2013) 103–108.
[11] A.C. Betz, S.H. Jhang, E. Pallecchi, R. Ferreira, G. Feve, J.M. Berroir, B. Placais, Supercollision cooling in undoped graphene, Nat. Phys. 9 (2013) 109–112.
[12] T.V. Alencar, M.G. Silva, L.M. Malard, A.M. de Paula, Defect-induced supercollision cooling of photoexcited carriers in graphene, Nano Lett. 14 (2014) 5621–5624.
[13] W. Chen, A.A. Clerk, Electron-phonon mediated heat flow in disordered graphene, Phys. Rev. B (2012) 86.
[14] C.B. McKitterick, D.E. Prober, M.J. Rooks, Electron-phonon cooling in large monolayer graphene devices, Phys. Rev. B 93 (2016).
[15] J. Yan, M.H. Kim, J.A. Elle, A.B. Sushkov, G.S. Jenkins, H.M. Milchberg, M.S. Fuhrer, H.D. Drew, Dual-gated bilayer graphene hot-electron bolometer, Nat. Nanotechnol. 7 (2012) 472–478.
[16] Q. Han, T. Gao, R. Zhang, Y. Chen, J.H. Chen, G.R. Liu, Y.F. Zhang, Z.F. Liu, X.S. Wu, D.P. Yu, Highly sensitive hot electron bolometer based on disordered graphene, Sci. Rep. 3 (2013).
[17] X. Cai, A.B. Sushkov, R.J. Suess, M.M. Jadidi, G.S. Jenkins, L.O. Nyakiti, R.L. Myers-Ward, S. Li, J. Yan, D.K. Gaskill, T.E. Murphy, H.D. Drew, M.S. Fuhrer, Sensitive room-temperature terahertz detection via the photothermoelectric effect in graphene, Nat. Nanotechnol. 9 (2014) 814–819.
[18] L. Vicarelli, M.S. Vitiello, D. Coquillat, A. Lombardo, A.C. Ferrari, W. Knap, M. Polini, V. Pellegrini, A. Tredicucci, Graphene field-effect transistors as room-temperature terahertz detectors, Nat. Mater. 11 (2012) 865–871.
[19] F.H.L. Koppens, T. Mueller, P. Avouris, A.C. Ferrari, M.S. Vitiello, M. Polini, Photodetectors based on graphene, other two-dimensional materials and hybrid systems, Nat. Nanotechnol. 9 (2014) 780–793.
[20] K.C. Fong, K.C. Schwab, Ultrasensitive and wide-bandwidth thermal measurements of graphene at low temperatures, Phys. Rev. X (2012) 2.
[21] K.C. Fong, E.E. Wollman, H. Ravi, W. Chen, A.A. Clerk, M.D. Shaw, H.G. Leduc, K.C. Schwab, Measurement of the electronic thermal conductance channels and heat capacity of graphene at low temperature, Phys. Rev. X (2013) 3.
[22] A.C. Betz, F. Vialla, D. Brunel, C. Voisin, M. Picher, A. Cavanna, A. Madouri, G. Feve, J.M. Berroir, B. Placais, E. Pallecchi, Hot electron cooling by acoustic phonons in graphene, Phys. Rev. Lett. 109 (2012).
[23] A. El Fatimy, R.L. Myers-Ward, A.K. Boyd, K.M. Daniels, D.K. Gaskill, P. Barbara, Epitaxial graphene quantum dots for high-performance terahertz bolometers, Nat. Nanotechnol. 11 (2016), 335-+.
[24] A. El Fatimy, A. Nath, B.D. Kong, A.K. Boyd, R.L. Myers-Ward, K.M. Daniels, M.M. Jadidi, T.E. Murphy, D.K. Gaskill, P. Barbara, Ultra-broadband photodetectors based on epitaxial graphene quantum dots, Nanophotonics 7 (2018) 735–740.
[25] Y.F. Yang, L.I. Huang, Y. Fukuyama, F.H. Liu, M.A. Real, P. Barbara, C.T. Liang, D.B. Newell, R.E. Elmquist, Low carrier density epitaxial graphene devices on SiC, Small 11 (2015) 90–95.
[26] F. Fromm, M.H. Oliveira, A. Molina-Sanchez, M. Hundhausen, J.M.J. Lopes, H. Riechert, L. Wirtz, T. Seyller, Contribution of the buffer layer to the Raman spectrum of epitaxial graphene on SiC(0001), New J. Phys. 15 (2013).
[27] L.G. Cancado, A. Jorio, E.H.M. Ferreira, F. Stavale, C.A. Achete, R.B. Capaz, M.V.O. Moutinho, A. Lombardo, T.S. Kulmala, A.C. Ferrari, Quantifying defects in graphene via Raman spectroscopy at different excitation energies, Nano Lett. 11 (2011) 3190–3196.
[28] D.K. Efetov, P. Kim, Controlling electron-phonon interactions in graphene at ultrahigh carrier densities, Phys. Rev. Lett. 105 (2010).
[29] K. Kaasbjerg, K.S. Thygesen, K.W. Jacobsen, Unraveling the acoustic electron-phonon interaction in graphene, Phys. Rev. B (2012) 85.
[30] K.M. Borysenko, J.T. Mullen, E.A. Barry, S. Paul, Y.G. Semenov, J.M. Zavada, M.B. Nardelli, K.W. Kim, First-principles analysis of electron-phonon interactions in graphene, Phys. Rev. B (2010) 81.
[31] M.M. Jadidi, J.C. Konig-Otto, S. Winnerl, A.B. Sushkov, H.D. Drew, T.E. Murphy, M. Mittendorff, Nonlinear terahertz absorption of graphene plasmons, Nano Lett. 16 (2016) 2734–2738.
[32] L.A. Falkovsky, A.A. Varlamov, Space-time dispersion of graphene conductivity, Eur. Phys. J. B 56 (2007) 281–284.
[33] C.H. Lui, K.F. Mak, J. Shan, T.F. Heinz, Ultrafast photoluminescence from graphene, Phys. Rev. Lett. 105 (2010).